Electronic Supplementary Material (ESI) for Nanoscale.

Supporting Information

Parameter Controls for Enhanced Peak-to-Valley Current Ratio in MoS_2/$MoTe_2$ van der Waals Heterostructure

Ngoc T. Duong[a,b], *Seungho Bang*[a,b], *Seung Mi Lee*[c], *Dang X. Dang*[a,b], *Dong H. Keum*[b], *Juchan Lee*[b], *Mun S. Jeong*[a,b,*] *and Seong C. Lim*[a,b,*]

[a] Department of Energy Science, Sungkyunkwan University, Suwon 16419, Republic of Korea

[b] Center for Integrated Nanostructure Physics, Institute of Basic Science (IBS), Sungkyunkwan University, Suwon 16419, Republic of Korea

[c] Korea Research Institute of Standards and Science (KRISS), Deajeon 34113, Republic of Korea

* Address correspondence to seonglim@skku.edu or mjeong@skku.edu

1. Optical images of $MoTe_2$ and MoS_2 flakes and the $MoS_2/MoTe_2$/hBN heterostructure.

Figures S1 (a) and (b) are optical images of the exfoliated $MoTe_2$ and MoS_2 flakes on poly vinyl-alcohol (PVA)/ poly methyl methacrylate (PMMA) spin coated on the Si/SiO_2 substrate. First, $MoTe_2$ and MoS_2 flakes were exfoliated on the PVA/PMMA substrate and the h-BN flake was exfoliated on the Si/SiO_2 substrate. After dissolving PVA by water, MoS_2 and $MoTe_2$ flakes remained on the surface of the PMMA sheet. Then, $MoTe_2$ and MoS_2 flakes were transferred on the top of h-BN flake.

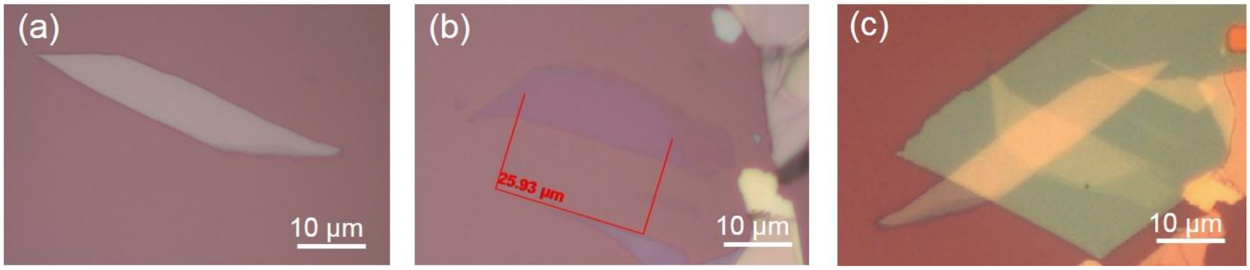

Fig. S1. (a) $MoTe_2$ and (b) MoS_2 flakes are mechanically exfoliated on a PVA/PMMA coating substrate. (c) $MoTe_2$ and MoS_2 heterostructure on a h-BN passivating layer.

2. Raman mapping of the peak positions of the A_{1g} and E_{2g} modes of the MoS_2 flake.

Scanning Raman spectroscopy of our sample was performed using NT-MDT (NTEGRA Spectra) over the overlapped and pristine area of MoS_2. Figure S2(a) is an optical image of the area to be examined using the instrument. The peak position of A_{1g} and E_{2g} modes were monitored inside the scanning area. The E_{2g} mode of the overlapped MoS_2 shows a redshift of ~ 1 cm^{-1} (from 381 cm^{-1} to 380 cm^{-1}) compared with the pristine one; this can be attributed to the strain effect of MoS_2 due to the interaction with the underlying $MoTe_2$ layer (Figure S2 (b)). The redshift of the E_{2g} mode by ~ 1 cm^{-1} indicates that the strain level exerted on MoS_2 is up to 1 %. The same analysis is applied on A_{1g} mode. A mapping image of the A_{1g} mode in Figure S2(c) demonstrates a redshift by ~ 1 cm^{-1} (406.6 cm^{-1} to 405.7 cm^{-1}), which can be attributed to the effect of electron transfer from the $MoTe_2$ to the MoS_2 layer. [1]

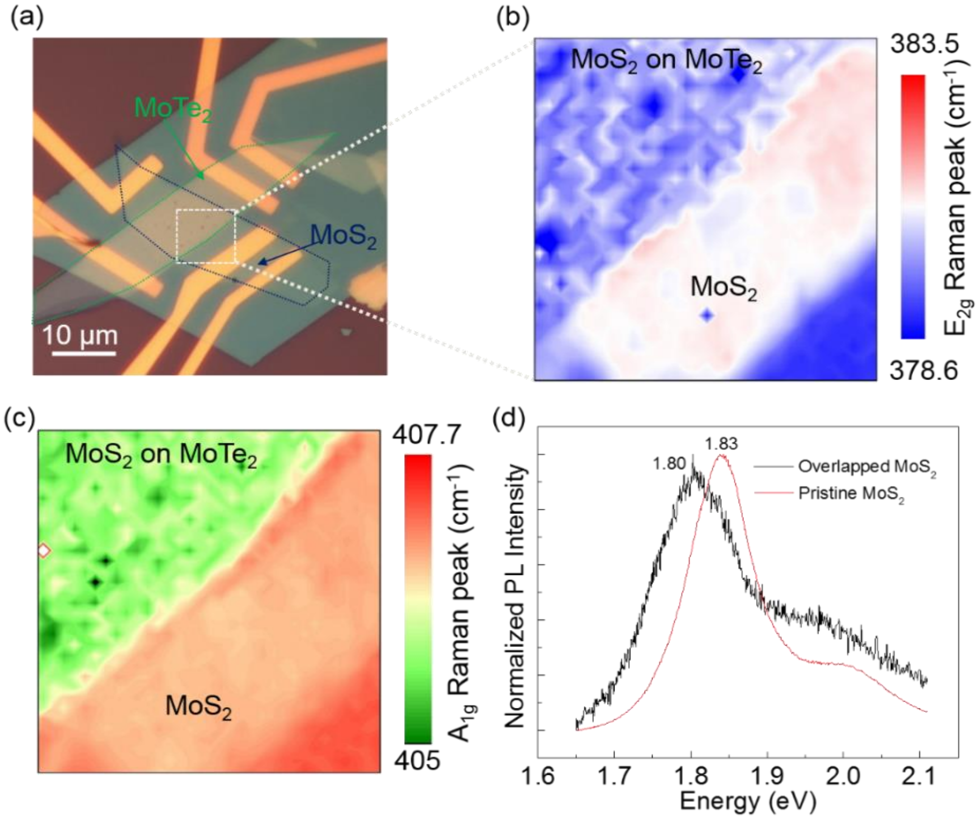

Figure S2. (a) MoS_2/$MoTe_2$ heterostructure with the scanning area. (b) E_{2g} and (c) A_{1g} Raman peak positions for the pristine and overlapped MoS_2 and $MoTe_2$ regions, respectively. (d) Arbitrary units PL spectra of pristine and overlapped MoS_2.

In addition to Raman peak analysis, the effect of strain is examined again using PL spectra. A room temperature photoluminescence (PL) spectrum is obtained in MoS_2 overlapped with $MoTe_2$ using NTMDT-NTEGRA system that is equipped with 532 nm wavelength laser. In the Fig. S2 (d), a significant redshift, approximately 30 meV, in the spectrum is observed, which strongly supports that MoS_2 is locally strained due to $MoTe_2$. The redshift of the A exciton peak by ~1 cm^{-1} results from the strain level of MoS_2 approximately 1 %.[1-3]

3. I–V characteristics of the $MoTe_2$ flake before and after BV doping.

We examined SiO_2 protection layer for $MoTe_2$ by BV using AFM. As shown in Fig. S3(a), SiO_2 covers uniformly $MoTe_2$ with the thickness of 100 nm. Hence, no direct doping of $MoTe_2$ by BV is expected to happen. However, a slight reduction of channel current is seen from the I_{ds}-V_{gs} curve in Fig. S3(b). In addition to it, a similar current decrease of channel current is also observed from I_{ds}-V_{ds} curves in Fig. S3(c) and S3(d). But, the overall linearity in the I_{ds}-V_{ds} in Figs. S3 (c) and S3(d) does not change. Hence, we expect that the current reduction in the figure is not because of doping of $MoTe_2$ by BV, but because of the dielectric properties of SiO_2 and BV, whose dielectric properties are quite different from the air. It is known that I-V properties are influenced by

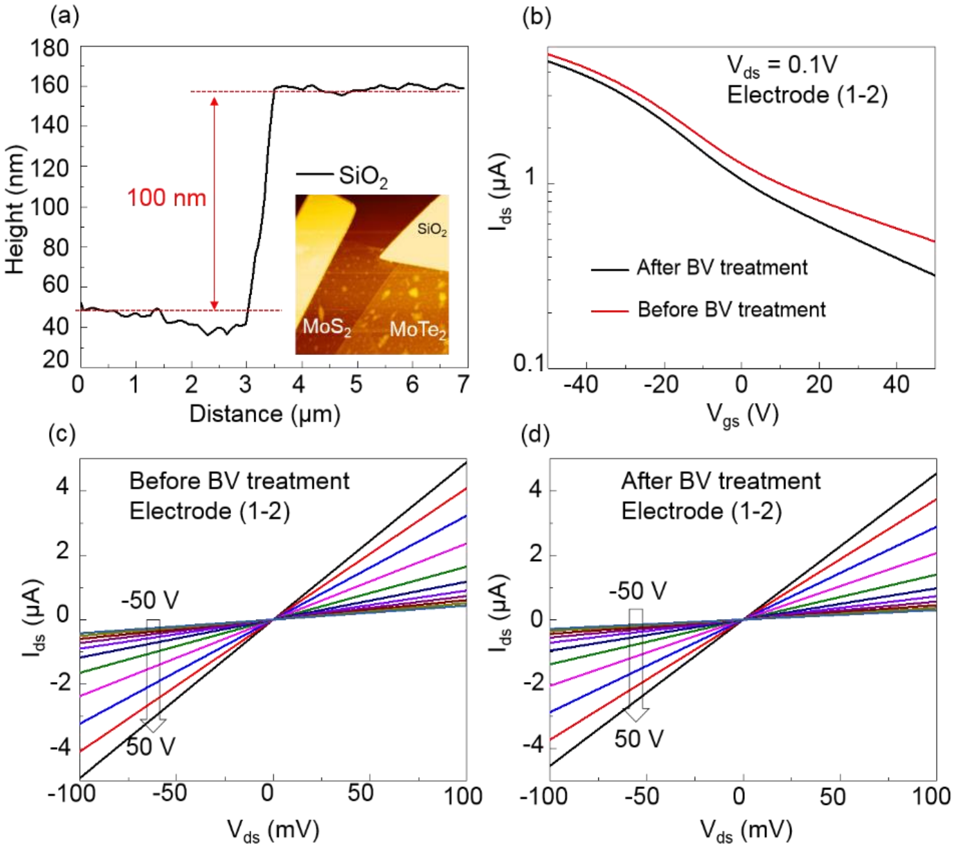

Figure S3. (a) Thickness profile of SiO_2 (b) I_{ds}–V_{gs} of the $MoTe_2$ flake after and before BV treatment. I_{ds}–V_{ds} of pristine $MoTe_2$ (c) after and (d) before BV treatment.

surrounding dielectric constant.[4] If the doping of $MoTe_2$ by BV occurred, then the p-type behavior of $MoTe_2$ would not be sustained after the BV doping that is a strong n-doping agent.

4. Temperature-dependence electrical characteristics of $MoS_2/MoTe_2$ heterostructure.

To further investigate the electrical transport in the doped $MoS_2/MoTe_2$ vertically stacked p-n diodes, we measured the temperature-dependent electrical properties, I_{ds}–V_{ds}. Figure S4a shows the I–V characteristics of the device in the temperature range of 60–300 K at V_{gs} = 0 V. All I–V curves show a rectifying behavior where the current range increases as a function of temperature in Fig. S4 (a) (shown in the semi-log plot in the inset). The current–voltage relation of the p-n diode can be described as

$$I = I_s[\exp\left(\frac{qV_{ds}}{nk_BT}\right) - 1] \tag{1}$$

where I_s is saturation current, V_{ds} is applied source-drain voltage, q is an electrical charge, n is the ideality factor, T is temperature, and k_B is Boltzmann's constant. To calculate the ideality factor (n) and Schottky barrier height (Φ_{SBH}), we take the log on both sides of equation (1), and we get

$$\ln(I) = \ln(I_s) + \left(\frac{q}{n\kappa_BT}\right)V_{ds} \tag{2}$$

When a semi-log plot of $ln(I)$ vs. V_{ds} is drawn, the slope is given as q/nkT and the intercept is $ln(I_s)$. By measuring the slope of $ln(I)$ vs. V_{ds}, n is obtained as a function of temperature from 1.5 at 300 K. n increases when the temperature is reduced, as shown in Figure S4b. Such a behavior is highly subject to the inhomogeneity of the Schottky barrier height.[5]

Determining the heterojunction barrier height is feasible using I_{ds}–T curves at a given V_{ds}, referring to the Richardson equation. The relationship (1) can be further described as follows:

$$\mathrm{I} = \mathrm{A}A^{*}T^{2}\exp\frac{e\emptyset_{SBH}}{kT}\left[\exp\left(\frac{qV_{ds}}{nk_{B}T}\right)-1\right], \tag{3}$$

where A is the Schottky junction area and A^{*} is the Richardson's constant. The Schottky barrier height is extracted from the saturation current I_S by

$$I_S = AA^{*}T^{2}\exp\left(-\frac{q\emptyset_{SBH}}{k_BT}\right) \tag{4}$$

After taking logs on both sides of Eq. (4), we get

$$ln\frac{I_s}{T^2} = \ln(AA^{*}) + \left(-\frac{q\emptyset_{SBH}}{k_BT}\right) \tag{5}$$

In this scenario, Φ_{SBH} can be estimated from Richardson's plot ($ln(I_S/T^2)$ vs. $1/T$) because the slope gives $-\frac{e\emptyset_{SBH}}{kT}$ and the intercept gives $ln\ (AA^{*})$. Our Richardson's plot is shown in Figure S4c

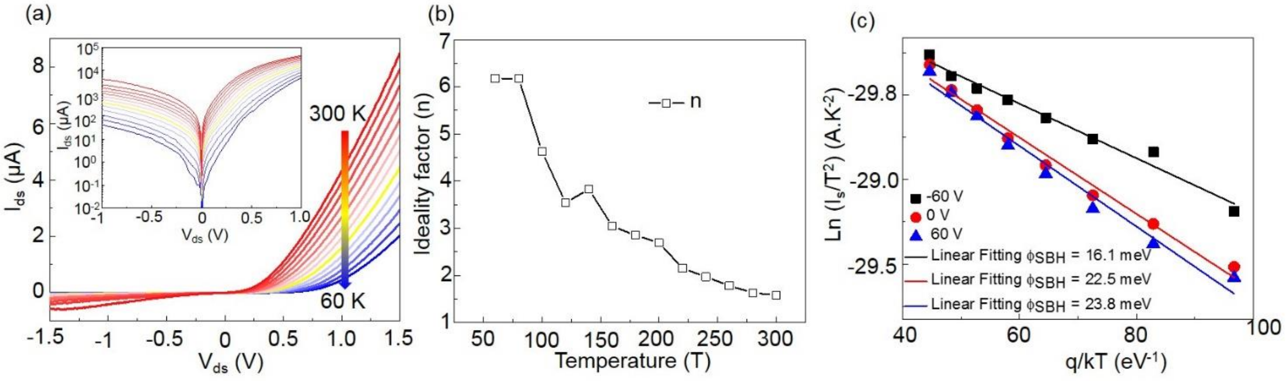

Figure S4. (a) I_{ds}–V_{ds} curve of the MoS_2–$MoTe_2$ diode at different temperatures (300 K–60 K). Inset: Semi-logarithmic plot of the same I_{ds}–V_{ds} curve. (b) Ideality factor (n) as a function of temperature. (c) The Richardson's plot of the doped MoS_2-$MoTe_2$ diode at different back-gate biases.

for different V_{GS} (−60 V, 0 V, and 60 V). The Φ_{SBH} estimated from the $MoS_2/MoTe_2$ junctions is ~ 16.1 meV, 22.5 meV, and 23.8 meV at V_{gs} = −60 V, 0 V, and 60 V, respectively. These estimated values are comparable to those in another report that comprised van de Waals MoS_2/BP heterojunction[6].

5. I_{ds}–V_{gs} curves of the $MoS_2/MoTe_2$ heterostructure with various V_{ds}

Figure S5 shows the I_{ds}–V_{gs} curves of the $MoS_2/MoTe_2$ heterostructure measured at different V_{ds}. All curves indicate n-type dominant characteristics and the current dips observed approximately at V_{gs} = –20 V become more apparent at higher V_{ds}.

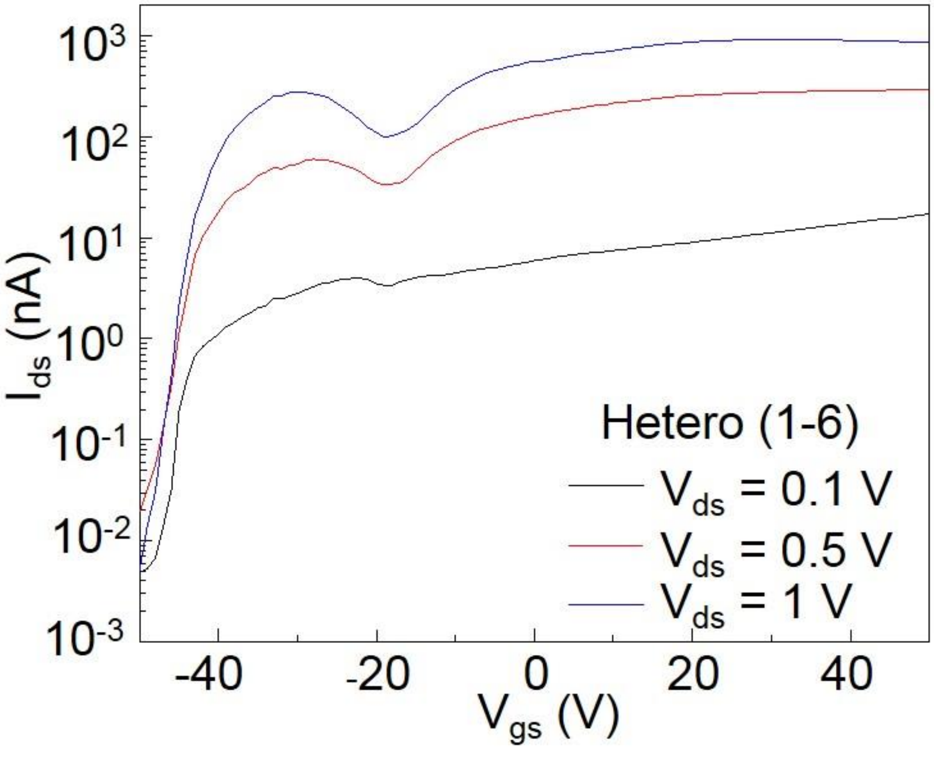

Figure S5. I_{ds}–V_{gs} curve of the $MoS_2/MoTe_2$ heterostructure.

6. Electrical characteristics of MoS_2 and $MoTe_2$ with different metal contacts.

Figure S6a shows the I_{ds}–V_{ds} of MoS_2 devices with Au and Ti metal contacts. In the case of the Au–MoS_2 contact, the curve shows non-linear behavior, while the Ti-MoS_2 contact show Ohmic-like linear behavior. This is due to the difference between the work function of MoS_2 and Ti; Au can form different metal-semiconductor contact types. Figure S6b shows the $MoTe_2$ with Au, Pd contacts. Both curves show Ohmic-like linear contacts; however, Pd-$MoTe_2$ devices have higher conductivity.

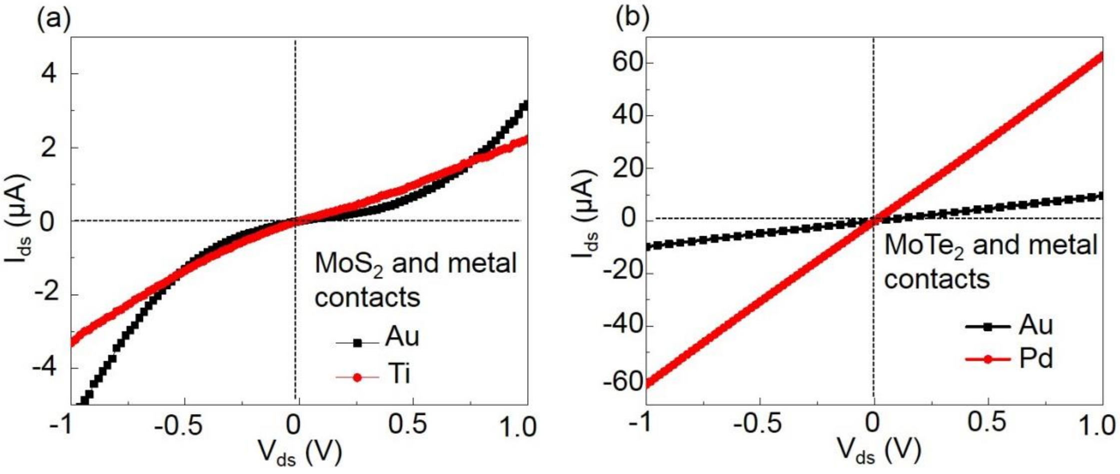

Figure S6. (a) MoS_2 devices with Au and Ti contacts. (b) $MoTe_2$ devices with Au and Pd contacts.

7. Thinning of the depletion region of the $MoS_2/MoTe_2$ heterostructure after doping by BV

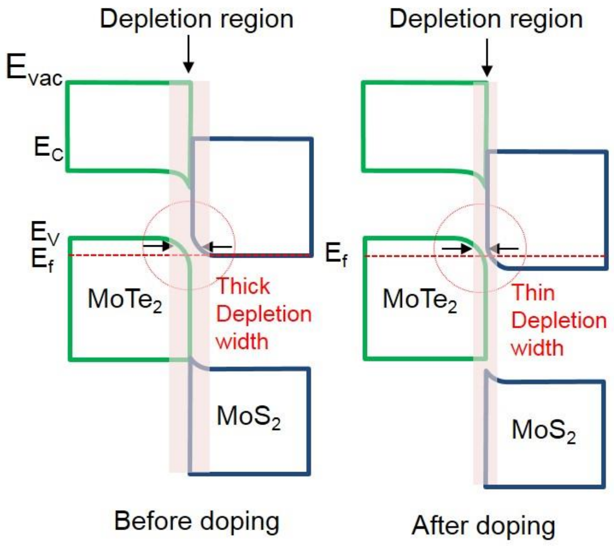

Figure S7. Depletion width of $MoS_2/MoTe_2$ heterostructure after and before BV doping.

Figure S7 shows the depletion region width in the p^+-n junction (before doping) and p^+-n^+ junction (after doping). The depletion width at the $MoS_2/MoTe_2$ heterointerface becomes narrower when the Fermi level of MoS_2 increases.[7]

8. Doping of MoS_2 by BV

Benzyl Viologen (BV) molecule shows itself as an effective molecule of electron donor for TMDs (Fig. S8 a). A complex of redox reaction is created based on the differences between the reduction potential of neutral BV molecules, -0.790 V (BV^0/BV^+) and -0332 (BV^+/BV^{2+}) and $E^C_{MoS_2}$~ 0 V vs. the standard hydrogen electrode (SHE), in Fig. S8 b.[8, 9] Due to the differences in energy level, two electrons are donated from BV^0 to MoS_2. Fig. S8c shows schematics of BV and electrons transfer to MoS_2 flakes. After the redox reaction, a complex between oxidized BV^{2+} and a divalent acceptor^{2-} is generated.

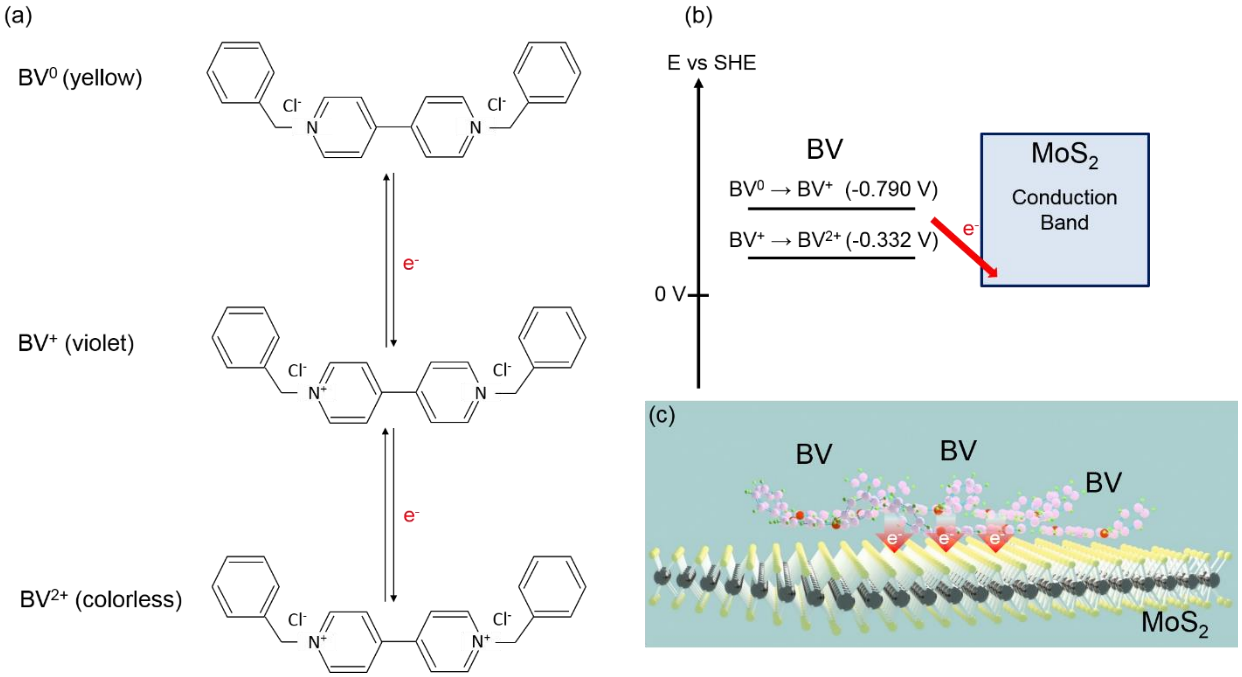

Figure S8. (a) Redox reaction of benzyl viologen molecules, (b) Energy band diagram of MoS_2 conduction band and redox states of BV, (c) A schematic of MoS_2, BV and electron transfer.

9. Calculation details

We performed quantum mechanical calculations within density functional theory (DFT) framework. Atomic orbital basis sets were used as implemented in DMOL3 code[10] in the double numerical with polarization with additional diffuse functions (DNP+). All electrons, including those from the core part, were considered during calculations. The exchange-correlation functionals using generalized gradient approximation (GGA)[11] and the *k*-points with Monkhorst-Pack grid with a separation of 0.02/Å were used. Geometry optimization criteria were 0.005 Å for distance, 0.001 Ha/Å for force, and 10^{-5} Ha for total energy difference.

The optimized bulk structures showed $a = b = 3.1212$ Å and $c = 11.8410$ Å for MoS_2 and $a = b = 3.5644$ Å and $c = 13.5313$ Å for $MoTe_2$ respectively. The calculated energy band gap using GGA-PBE functional were 1.067 eV for MoS_2 and 0.777 eV for $MoTe_2$. Comparing to the experimental values $a = b = 3.161$ Å and $c = 12.295$ Å for MoS_2 $a = b = 3.519$ Å and $c = 13.964$ Å for $MoTe_2$, our method represents in reasonable agreement. The underestimation of band gap by DFT calculation is well known. The difference of calculated band gaps between MoS_2 and $MoTe_2$ was 0.29 eV, close to that of measured value of ca. 0.3 eV. Calculation data with comparison to the experimental data for bulk systems are summarized in Table S1.

From the optimized bulk structure, we generated multi-layered structure and calculate the electronic structures. We applied vacuum region as 15 Å in order to avoid any artificial inter-supercell interaction.

Table S1. The calculated lattice constants and the electronic energy gap. All electron density functional theory calculations using GGA-PBE functional were used.

	MoS_2/PBE		MoS_2/Expt.		$MoTe_2$/PBE		$MoTe_2$/Expt.	
Lattice const.(Å)	a	c	a	c	a	c	a	c
	3.1212	11.8410	3.161	12.295	3.5644	13.5313	3.519	13.964
E_{gap} (eV)	1.067		1.23 [12]		0.777		0.88 [13]	

Table S2. The calculated energy levels using all electron density functional theory scheme. The reference was set to the Fermi level of the 13-layer $MoTe_2$ supercell. VBM and CBM represent the valence band maximum and the conduction band minimum, respectively. We used 15 Å of vacuum in the calculation.

	$MoTe_2$ 13-layerd	**MoS_2 5-layered**
E_{Fermi} (eV)	0	-0.309
E_{gap} (eV)	0.779	1.137
VBM (eV)	-0.182	-0.662
CBM (eV)	0.597	0.475
Height (Å)	87.9535 + vacuum	29.6025 + vacuum

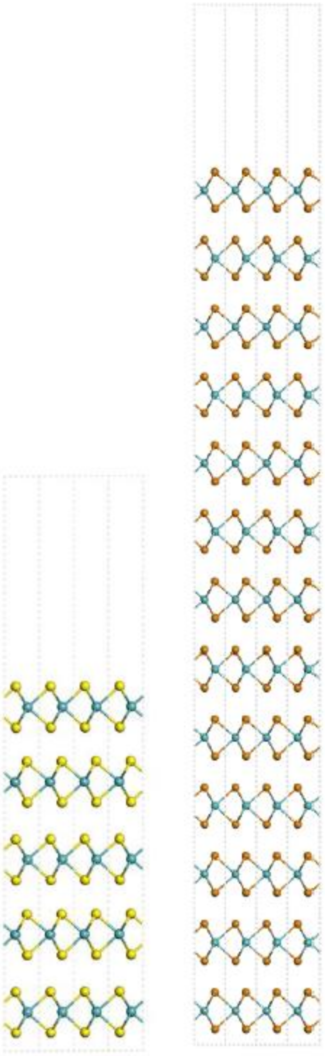

Figure S9. The calculated supercells, i.e., 5-layered MoS_2 (left) and 13-layered $MoTe_2$ (right) in ball and stick form.

Supplementary References:

1 B. Chakraborty, A. Bera, D. V. S. Muthu, S. Bhowmick, U. V. Waghmare and A. K. Sood, *Phys. Rev. B - Condens. Matter Mater. Phys.*, 2012, **85**, 161403.

2 A. Castellanos-Gomez, R. Roldán, E. Cappelluti, M. Buscema, F. Guinea, H. S. J. Van Der Zant and G. A. Steele, *Nano Lett.*, 2013, **13**, 5361–5366.

3 H. J. Conley, B. Wang, J. I. Ziegler, R. F. Haglund, S. T. Pantelides and K. I. Bolotin, *Nano Lett.*, 2013, **13**, 3626–3630.

4 D. Kufer and G. Konstantatos, *Nano Lett.*, 2015, **15**, 7307–7313.

5 D. Subba Reddy, M. Siva Pratap Reddy and V. Rajagopal Reddy, *Optoelectron. Adv. Mater. Rapid Commun.*, 2011, **5**, 448–454.

6 J. Miao, Z. Xu, Q. Li, A. Bowman, S. Zhang, W. Hu, Z. Zhou and C. Wang, *ACS Nano*, 2017, **11**, 10472–10479.

7 D. K. Schroder, *Semiconductor Material and Device Characterization: Third Edition*, 2005.

8 S. Mouri, Y. Miyauchi and K. Matsuda, *Nano Lett.*, 2013, **13**, 5944–5948.

9 D. Kiriya, M. Tosun, P. Zhao, J. S. Kang and A. Javey, *J. Am. Chem. Soc.*, 2014, **136**, 7853–7856.

10 B. Delley, *J. Chem. Phys.*, 2000, **113**, 7756–7764.

11 J. Perdew, K. Burke and M. Ernzerhof, *Phys. Rev. Lett.*, 1996, **77**, 3865–3868.

12 K. K. Kam and B. A. Parkinson, *J. Phys. Chem.*, 1982, **86**, 463–467.

13 I. G. Lezama, A. Ubaldini, M. Longobardi, E. Giannini, C. Renner, A. B. Kuzmenko and A. F. Morpurgo, *2D Mater.*, 2014, **1**, 21002–13.